Evidence of cationic antiphase disorder in epitaxial Cu(In,Ga)S_2 grown on GaP/Si(001)

Eugène Bertin, Eric Gautron, Nicolas Barreau, C. Cornet, Ludovic Arzel, Léo Choubrac, Antoine Létoublon, Sylvie Harel, Rozenn Bernard, Maud Jullien, et al.

Evidence of cationic antiphase disorder in epitaxial $Cu(In,Ga)S_2$ grown on GaP/Si(001)

Eugène Bertin[a,b], Éric Gautron[b], Nicolas Barreau[b], Charles Cornet[a], Ludovic Arzel[b], Leo Choubrac[b], Antoine Létoublon[a], Sylvie Harel[b], Rozenn Bernard[a], Maud Jullien[a], Rohel Tony[a], Lionel Assmann[b], Olivier Durand[a]

[a] *Univ Rennes, INSA Rennes, CNRS, Institut FOTON - UMR 6082, F-35000 Rennes, France*

[b] *Nantes Université, CNRS, Institut des Matériaux de Nantes Jean Rouxel – UMR6502, F-44000 Nantes, France.*

1 List of Abbreviations

CIGS $Cu(In,Ga)S_2$

CIS $CuInS_2$

CGS $CuGaS_2$

SLG Soda lime glass

CH Chalcopyrite

TS Thiospinel

TEM Transmission electron microscope

CA CuAu

ACOM Automated crystal orientation mapping

ED Electron diffraction

HR High resolution

STEM Scanning transmission electron microscope

HAADF High-angle annular dark field

GPA Geometric phase analysis

ZB Zinc-blende

EDX Energy dispersive X-ray spectroscopy

APD Antiphase disorder

CAPD Cation antiphase disorder

CAPB Cation antiphase boundary

2 Abstract

We present a transmission electron microscopy study of epitaxial $Cu(In,Ga)S_2$ (CIGS) films co-evaporated on GaP/Si(001), in either Cu-rich or Cu-poor conditions. We first unveil the spatial distribution and the orientation of the different phases by means of electron

diffraction. From atomically resolved imaging of the CIGS film's atomic structure, we conclude that different chalcopyrite domains, sharing cation antiphase symmetries of the cation sublattice, coexist in the films. We conceptualize at least three types of cation antiphase boundaries (CAPBs), which does or does not lead to a violation of the octet rule, depending on the propagation direction. Even though we observe that epitaxial CIGS is highly prone to cation antiphase disorder, we find that the growth of CIGS in Cu-rich conditions leads to a lower density of CAPBs, as compared to Cu-poor growth conditions. This opens the question of the influence of CAPBs on CIGS electronic properties.

3 Introduction

$Cu(In,Ga)S_2$ (CIGS) compounds offer tunable bandgaps between 1.54 eV for $CuInS_2$ (CIS) to 2.43 eV for $CuGaS_2$ (CGS) [1], making them suitable for single-junction and tandem solar cells. Integrating CIGS on crystalline Si (c-Si) in a 2-terminal monolithic configuration is a practical approach for cost-effective, high-efficiency solar cells [2–4]. Namely, the $CuIn_{0.75}Ga_{0.25}S_2$ chalcopyrite displays a near ideal bandgap of 1.7eV for a top cell absorber. Recent advancements in CdS/CIGS [5] and Zn(O,S)/CIGS [6] heterojunction solar cells on Mo-coated soda-lime glass (SLG) substrates have achieved efficiencies over 15%. However, translating these achievements to Si-based tandem cells introduces several challenges, such as replacing the opaque Mo/SLG substrate with a Si substrate, controlling the diffusion of Cu in the Si [7] and establishing an optimal interconnect between wide-bandgap CIGS and Si [8].

Our method involves the deposition of wide bandgap chalcopyrite films by coevaporation on a GaP/Si(001) pseudo-substrate [9,10]. GaP exhibits quasi-lattice matching with Si, with a small lattice mismatch of 0.37% at room temperature [11]. The chalcopyrite $CuIn_{0.75}Ga_{0.25}S_2$ film, with a bandgap of 1.7 eV, exhibits a crystal symmetry and lattice parameters close to that of zinc-blende GaP and diamond Si. Introducing a thin GaP interlayer offers three main advantages. Firstly, the GaP interlayer triggers the epitaxy of CIGS on Si(001), promoting the formation of a high-quality, dense, and adherent CIGS film with a minimal density of grain boundaries [9]. Secondly, we postulate that the GaP layer acts as a diffusion barrier, preventing the migration of potentially harmful species such as Cu from the CIGS to the Si. Thirdly, GaP has a low absorption coefficient [12] due to its 2.26 eV indirect bandgap [13], and an electron affinity of 3.8 eV [14]. This aligns the valence band of GaP with that of CIGS (assuming an electron affinity of 4.7 eV [15,16] for CIGS), making GaP an ideal passivating selective contact for holes. For further details, refer to our recent articles on the growth of wide bandgap CIGS and $CuGaSe_2$ on GaP/Si(001) [9,10].

In a recent article [9], we studied the influence of the Cu content on the phase stability and the orientation of CIGS films grown on GaP/Si(001) by one-stage process [9]. We showed that, in the Cu-poor sample, the predominant chalcopyrite (CH) CIGS phase coexists with the thiospinel (TS) $CuIn_5S_8$ and a very small fraction of CuAu-ordered (CA) CIS. On the other hand, the KCN-etched Cu-rich sample was demonstrated to be monophasic with the CH crystal structure. All phases described here were found to share an epitaxial relationship with each other and with the GaP/Si(001) pseudo-substrate. We demonstrated the unicity of the CH crystal orientation in both cases, with the c-axis in the growth direction. Higher correlation lengths were measured by X-ray diffraction in Cu-rich conditions as compared to

the sample grown in Cu-poor conditions. This demonstrated a higher crystallinity in the Cu-rich sample; as compared to the Cu-poor sample, despite the epitaxial texture of both samples. This raises the question of the type of defects present in epi-CIGS films.

Only a handful of 2D extended defects are reported in epitaxial CH crystals grown on zinc-blende (ZB) III-V substrates, namely (i) boundaries between orientation domains with c-axis pointing in different directions [17], which we showed are absent in our samples [9], and (ii) cation antiphase boundaries [17,18] between CH domains sharing translational symmetries of the cation sublattice. In particular, cation antiphase boundaries in $Cu(In,Ga)Se_2$ have been studied theoretically [19] and experimentally [18], and have been shown, by means of cathodoluminescence, to have minimal electrical activity. However, to the best of our knowledge, minimal research has been directly towards the study of cation antiphase disorder in CIGS sulfides. In this article, we evidence cation antiphase boundaries in CIGS by means of atomically resolved scanning transmission microscopy and evaluate the influence of the Cu content during the deposition process on cationic antiphase disorder.

4 Methods

4.1 Epitaxial growth of GaP on Si(001) substrates: molecular beam epitaxy.

A 30nm-thin pseudomorphic GaP layer is epitaxially grown on p-type Si substrate with a 6° offset towards [110] at 500°C using a solid-source molecular beam epitaxy reactor [20]. More details can be found in Ref. [9].

4.2 Physical vapor coevaporation of CIGS films

Two CIGS samples are coevaporated using 1-stage process on the same GaP/Si(001) platform. The Cu-poor sample is grown in Cu-deficient conditions and investigated as grown. The Cu-rich sample is grown in Cu-excess conditions, and subsequently undergoes a 2 min KCN etching process in aqueous solution to remove $Cu_{2-x}S$ clusters from the surface. More details on the samples can be found in Ref. [9].

4.3 Transmission electron microscopy

All the transmission electron microscopy (TEM) experiments were performed on the same apparatus: a Cs-probe corrected Themis Z G3 (Thermo Fisher Scientific) operating at 300 kV accelerating voltage.

4.3.1 Sample preparation

Pieces of samples (≈ 3 x 0.5 mm^2) were cut with a diamond wire saw along the Si[010] direction. TEM cross-sectional specimens were prepared by mechanical polishing (down to 10 µm thick) followed by argon beam ion milling (Gatan PIPS 691) at low voltage (from 3 kV to 100 V at the final step) and low temperature (-40°C) to limit sample degradation and Cu diffusion.

We specifically choose the <100> zone axis to probe the crystal by electron diffraction (ED) and to observe the atom ordering by mean of high angle annular dark field (HAADF)-scanning transmission electron microscopy (STEM). This choice of zone-axis, which does not

correspond to a natural cleavage direction of the Si, is motivated by the observation of the CH-exclusive ordering of the cation sublattice. Indeed, in the <100> zone-axis, the CH exhibits special crystallographic features corresponding to the ordering of the cations in the form of Cu or (In,Ga) dimers orientated in the [001] direction, when projected onto (100). Indeed, these fine details of the CH structure cannot be probed in the <110> zone-axis as the symmetry of the CH in the latter zone-axis is extremely similar to that of the zinc-blende structure. This makes the CH harder to distinguish from the GaP in the <110> zone-axis.

4.3.2 Atomically resolved STEM imaging

HAADF-STEM images have been acquired with a 21.4 mrad convergence angle and 63 – 200 mrad collection angles, and simulated with the Dr. Probe software [21].

4.3.1 Geometric phase analysis

Geometric phase analysis (GPA) has been performed on high resolution (HR)-HAADF images thanks to GPA software [23], developed as a plugin for the commercial software DigitalMicrograph from Gatan Inc. GPA is usually used for the study of strain. In this work, it allowed to evidence defects in the cationic sublattice in the CIGS crystal. Details can be found in SI, Figure S4.

4.3.2 Automated crystal orientation mapping

Automated Crystal Orientation Mapping (ACOM) tool (ASTAR, Nanomegas) was used to reveal orientation and phase distribution in the samples. In TEM mode, we scan a predefined area with the electron beam and acquire an ED pattern for each 10nm pixel. The 2 – 3 nm electron beam was quasi parallel (TEM microprobe, spot size 10, 10 µm condensor aperture). Experimental ED patterns at each location are compared with the calculated patterns of CH-CIGS, TS-$CuIn_5S_8$, GaP and Si [22] for different orientations (see Ref. [9] for details on the discussed phases). This template matching yields both the orientation and phase maps at each pixel of the map. The choice of candidate crystals is based on our X-ray study of the Cu-poor and Cu-rich CIGS films on GaP/Si [9].

4.3.3 Energy-dispersive X-ray spectroscopy

Energy dispersive X-ray spectroscopy (EDX) maps were acquired with 4 windowless silicon drift detectors (Bruker detectors, Super-X system) [24]

5 Results and Discussion

The HAADF-STEM image of the Cu-rich lamella sample can be found in SI **Erreur ! Source du renvoi introuvable.**. Large crevices, 500 to 1000nm in depth, are found. These crevices result from the KCN etching of the $Cu_{2-x}S$ secondary phase. Indeed, the locations occupied by $Cu_{2-x}S$ clusters in the as-grown film yield large crevices after the chemical etching. Conversely, the Cu-poor sample is observed to be dense, without any crevices (data not shown).

5.1 Orientation mapping and secondary phase distribution

To study the orientation of the Cu-rich and Cu-poor CIGS films and the distribution of secondary phases within them, we conducted an ACOM experiment (see Section 4.3.1). The results are presented in Figure 1 for the Cu-rich and Cu-poor CIGS samples. In the phase

maps of Figure 1(c)(f), each phase is assigned a color. Pixels at which the phase identification is less reliable appear in darker shades of the corresponding color. At the interfaces, where diffraction signal from two phases may coexist, the reliability is lower. Thus, dark pixels clearly delineate the interfaces between the different crystal phases.

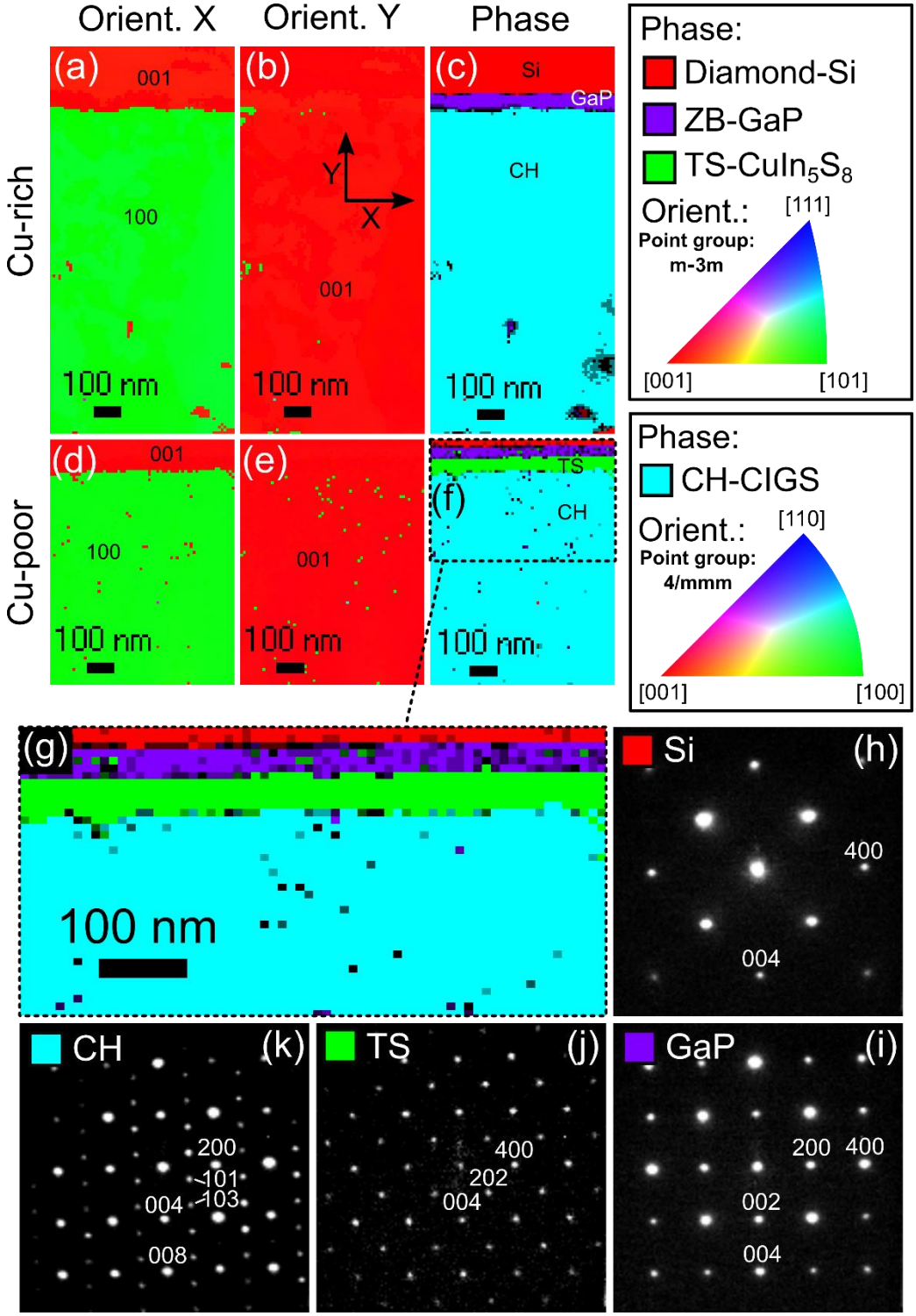

Figure 1: Orientation map (a)(d) along X, (b)(e) along Y and (c)(f) phase map for the (d)(e)(f) Cu-poor and (a)(b)(c) Cu-rich sample. (g) Zoom around the GaP layer for the Cu-poor sample. Electron diffraction pattern of (h) the Si, (i) the GaP, (j) the TS and (k) the CH phases.

The Cu-poor CIGS sample phase map extracted from the ACOM measurement is displayed in Figure 1(f). The matching algorithm yields the following results, from top to bottom: diamond Si, ZB-GaP, TS-$CuIn_5S_8$ and CH-CIGS. A close-up view of the region of Cu-poor sample's exhibiting TS-$CuIn_5S_8$ is presented in Figure 1(g), from which we extracted raw ED patterns. To validate the algorithmic matching of the block data, we included the experimental diffraction patterns in Figure 1(h–k) for the Cu-poor sample. All patterns correspond to the theoretical patterns in the <100> zone-axis of the identified phases, as simulated with PTCLab [25] (see **Erreur ! Source du renvoi introuvable.**(d)). The presence of TS-$CuIn_5S_8$ in the Cu-poor sample was previously demonstrated by X-ray diffraction [9]. The novelty is that we show that the TS-$CuIn_5S_8$ is shown to crystallize in-between the GaP and CH-CIGS. To confirm the presence of the TS-$CuIn_5S_8$, we used STEM-EDX, as shown in SI **Erreur ! Source du renvoi introuvable.**. Relative to the stoichiometry of the CH, we reveal a Cu-poor, In-rich and Ga-free layer between the CIGS and the GaP, in the Cu-poor sample, which perfectly fits the expected chemical fluctuations for a TS-$CuIn_5S_8$ film. In a previous study [9], we detected the presence of CuAu-ordered crystallites in the Cu-poor CIGS sample. Using TEM, we do not find any crystallites that would match the electron simulated ED pattern of CuAu-ordered CIGS. This absence may stem from the small volume of CA crystallites [9], preventing their detection.

The crystallographic orientation along the X and Y axes, corresponding to the edges of the scanned region, can be read in Figure 1(d) and (e) respectively, for the Cu-poor sample. Si, GaP and TS-$CuIn_5S_8$ belong to the cubic $m\bar{3}m$ Laue group, and their orientation can be read on the corresponding orientation diagram. CH-CIGS belongs to the tetragonal $4/mmm$ Laue group, so its orientation must be read on a different orientation diagram. The orientation of all the phases of Laue group $m\bar{3}m$ is [001] along X and Y. [001] is equivalent to the [100] and [010] orientation in a cubic crystal. The orientation of CH-CIGS of Laue group $4/mmm$ is [100] along X, which is equivalent to [010]. Along Y, CH-CIGS adopts the [001] orientation, indicating that the *c* of the tetragonal lattice is oriented along the growth direction. This orientation map result is validated by the indexation of raw diffraction patterns in Figure 1(h–k) for the Cu-poor sample. Indeed, in the CH-CIGS diffraction pattern of Figure 1(k), we observe (10l) reflections with l odd, which are exclusive to the CH original cation sublattice ordering. These reflections lines point towards the *c* axis, or [001] direction, of the tetragonal lattice, as shown in **Erreur ! Source du renvoi introuvable.**(e). For the Cu-poor sample, the orientation map demonstrates unambiguously that the epitaxial relationship between the phases is as follows: CH[100](001)//TS[100](001)//GaP[100](001)//Si[100](001). When shifting our attention to the phase and orientation distribution of the Cu-rich sample, we see in Figure 1(c) that the TS-$CuIn_5S_8$ is absent in the Cu-rich sample, in accordance with Ref. [9]. Therefore, the epitaxial relationship deduced in Figure 1(a)(b) is the same, with the exception that the TS-$CuIn_5S_8$ is absent.

So far, we have determined the orientation and location of the different phases. In both cases, the main phase is shown to be a CH crystal with a unique orientation. However, to get insights into defects of the cation sublattice, a finer characterization using high-resolution (HR) HAADF-STEM imaging in necessary.

5.2 High-resolution imaging of the CIGS/GaP interface

Atomically resolved HR-STEM images at the CIGS/GaP interface are displayed in Figure 2(a-c) for the Cu-poor sample and Figure 2(d-f) for the Cu-rich sample. Note that full scale HR-STEM images are available for download in SI.

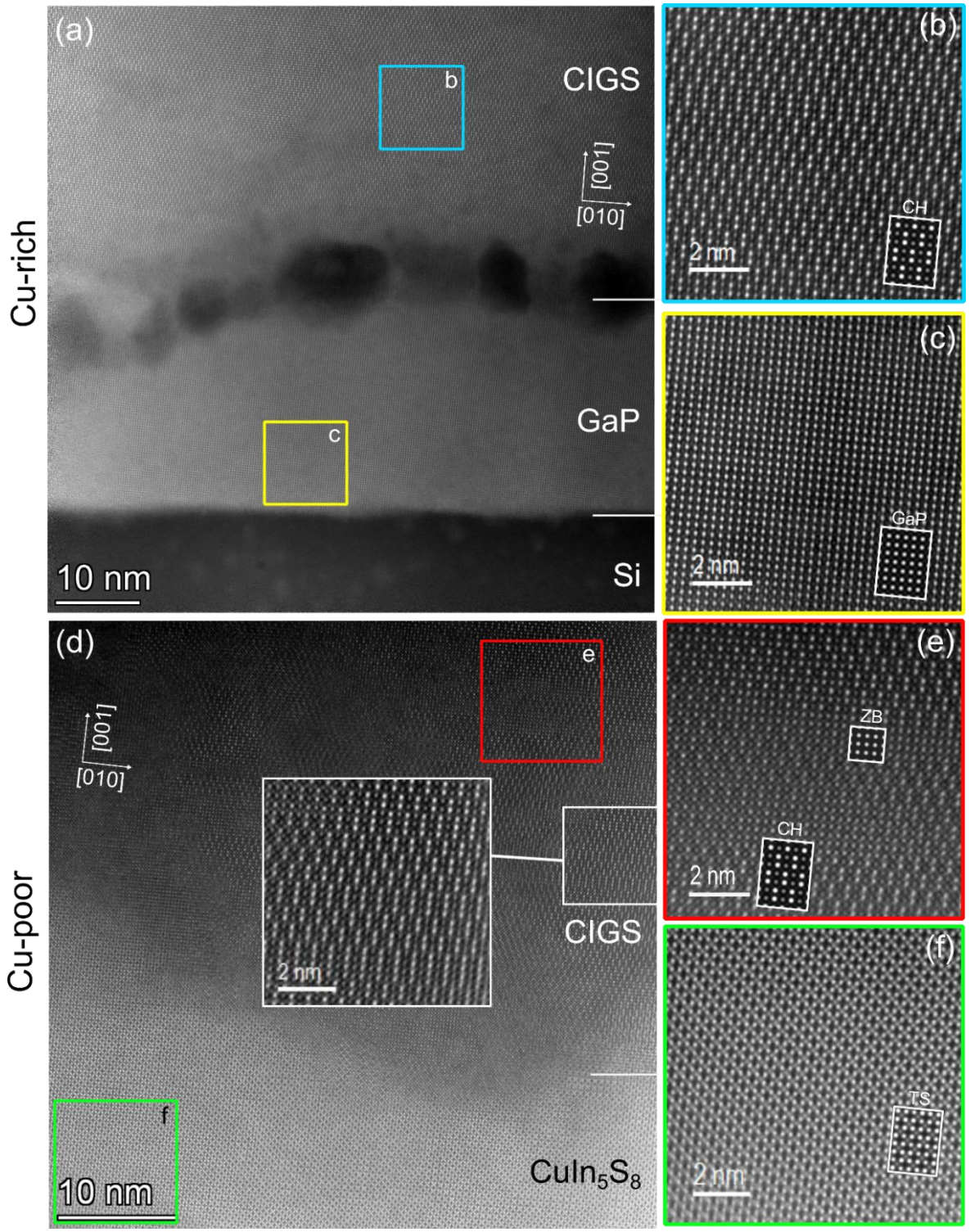

Figure 2: HAADF-HR-STEM image of the (a)(b)(c) Cu-rich and (d)(e)(f) Cu-poor sample. (b)(c)(e)(f) Wiener-filtered zoom at the locations of the rectangles of the matching color. Inset: Simulated

HAADF-STEM images for (b) CH-CIGS (c) GaP and (f) TS-$CuIn_5S_8$ and for (e) CH-CIGS and ZB-CIS. (d) Inset: Zoom in the region marked by the white square.

In the Cu-rich sample, the image in Figure 2(a) includes the CH-CIGS, GaP and Si. Close-up views of the apparent atomic ordering are visible in Figure 2(b) and (c) for CIGS and GaP, respectively. One can clearly see that the pseudo-cubic atomic structure of the CIGS and the cubic structures of GaP and Si are resolved simultaneously in the <100> zone axis. HR-STEM simulations for CH-CIGS, TS-$CuIn_5S_8$, and GaP are shown in subfigures insets, showing good matching with the experimental data. In STEM-HAADF the collected dark-field signal increases with the atomic number Z of the atom as about $Z^{1.7}$ [26]. This allows for the direct identification of the chemical nature of individual atomic sites. In GaP, one may recognize its cubic lattice, with heavier Ga atoms appearing bright and P atoms being almost indiscernible. This atomic ordering is the expected structure of GaP in the <100> zone-axis. In CH-CIGS, heavier III cations corresponding to (In,Ga) appear brighter while lighter Cu atoms appear darker. Similarly to P anions in GaP, S anions are too light to be clearly visible. In Figure 2(b), III=(In,Ga) cations and Cu cations are organized in the form of pairs orientated in the vertical direction, which is a characteristic of the CH structure. By comparison with the simulated HR image of the CH crystal in Figure 2(b) Inset, for the same <100> zone-axis, one can identify the direction of the cationic pairs to be the *c*-axis of the CH crystal. In Figure 2(a), for the Cu-rich sample, the CIGS and GaP layers are separated by a dark region, where no structure can be resolved. An additional close-up unfiltered HR image of the CIGS/GaP interface is available in **Erreur ! Source du renvoi introuvable.**(b). The dark regions correspond to voids, at the CIGS/GaP interface. Despite the voids, crystallographic orientation of GaP is indeed transmitted through the interface, to the CH-CIGS.

For the Cu-poor sample, we display the HR-STEM image of the CH-CIGS/$CuIn_5S_8$ interface in Figure 2(d-f). In the lower region of the image, the crystal ordering perfectly matches that of TS-$CuIn_5S_8$, as simulated in Figure 2(f) Inset, for the <100> zone axis. See **Erreur ! Source du renvoi introuvable.** and **Erreur ! Source du renvoi introuvable.** for more details. The characteristic vacant crystallographic sites of the TS structure are clearly visible, in the form of black voids within the TS-$CuIn_5S_8$ structure. Based on HR-STEM image of **Erreur ! Source du renvoi introuvable.**, we determine the thickness of the $CuIn_5S_8$ layer to be 20 – 26nm. Across the interface in Figure 2(d), towards the CIGS side, one can notice a disturbed crystal phase, which does not match the atomic ordering of the CH in every location. Since the $CuIn_5S_8$ crystal structure below is accurately resolved, we exclude scanning problems as a reason for such an effect. We argue that it is indeed a characteristic of the Cu-poor CH-CIGS crystal. In the upper-right part of Figure 2(e), we recognize the crystal structure of the expected CH crystal with its *c*-axis orientated in the growth direction, as simulated in Figure 2(e) Inset. However, such CH domains appear to be about 5 – 10 nm in size. Indeed, when scanning away from the CH domain with the eye, the atomic ordering seems to change. Other regions of Figure 2(e) are characterized by an apparent “ZB-type” ordering. In these regions, we cannot clearly distinguish III and Cu atoms in the structure. However, it is unlikely that such a ZB-CIS phase is present, since it is reported to be theoretically unstable at room temperature [27].

5.3 Cation antiphase disorder in epitaxial CIGS

Broadly speaking, if the CH domains are small, several domains may be present in the plane of the image, or in the depth of the lamella. In HR-STEM images, the third dimension of the lamella depth is projected onto the two dimensions of the STEM image. Hereafter, we use the same principle and measure distances in projection onto the plane of the STEM image. We now only consider the cation sublattice of the CH structure. One can hypothesize that different cationic sublattice domains may share translational symmetries. For example, they may be related by a translation of a cation-to-cation distance. Given the symmetry of the CH cation sublattice, two non-equivalent domains in addition to the identity domain may arise and are presented in Figure 3. CH domains may undergo a translation of a distance +c/4 along [001] or +a/2 along [010].

At this stage, it is important to clarify one thing. One could argue that such disorder could be referred to as antiphase disorder (APD). However, in the GaP/Si community, APD has a very precise meaning corresponding to the coexistence within the GaP film of two kind of cubic ZB domains, sharing inversion symmetry i.e. where all Ga and P atoms are replaced with P and Ga atoms respectively [28,29]. For clarity, the type of defects in the cationic sublattice discussed in this work will be referred to as cationic antiphase disorder (CAPD), to avoid confusion with APD. APD and CAPD of the cationic sublattice are different in that the former deals with variation in the cation-to-anion symmetry, while the latter is strictly limited to the cation sublattice. Indeed, in CAPD, the S anionic sublattice stays relatively unaffected, and anion-to-cation ordering is satisfied. CAPD has been experimentally observed in epitaxial Cu(In,Ga)Se_2, $MgFe_2O_4$ and $SrTiO_3$:Sn grown on GaAs [17,18], MgO(001) [30] and $SrTiO_3$ respectively, and in other types of materials like $MgAl_2O_4$ and $BeAl_2O_4$ [31].

In the following, we first focus on the Cu-poor epi-CIGS sample, to introduce the concepts associated with CAPD, and to describe two kinds of crystallographic defects. Then, we will shift our attention to the Cu-rich epi-CIGS sample, which will allow us to study a third kind of defect. After that, we will compare the two samples and discuss the differences between them.

5.3.1 Cation antiphase disorder in Cu-poor epi-CIGS

As sketched in Figure 3(g), if the base domain and a “c/4-translated” domain are both present in the depth of the TEM lamella, some columns contain both Cu and III atoms, and thus appear in an intermediate shade of gray. We simulate such a defect with a crystal model where two equally sized cation sublattice domains sharing a +c/4 translational symmetry are placed in the depth of the lamella i.e., along [100]. Based on this simulation, this should yield an HR image presented in Figure 3(f). We would observe bright III atoms hexagonally distributed on the cation sublattice, laterally separated by dark Cu atoms. Planes of mixed III/Cu atoms of intermediate shades of gray are found in between, and stack in the [001] direction. The atomic ordering visible in the top-left corner of Figure 2(e), and in Figure 3(c) precisely corresponds to this description. This demonstrates that several CH domains, whose cation sublattice shares cation antiphase symmetries can be found within the depth of the lamella sample, in the case of the Cu-poor sample. This apparent ordering

will be referred to as “Hex-type” in the following, based on the hexagonal position of the bright atoms.

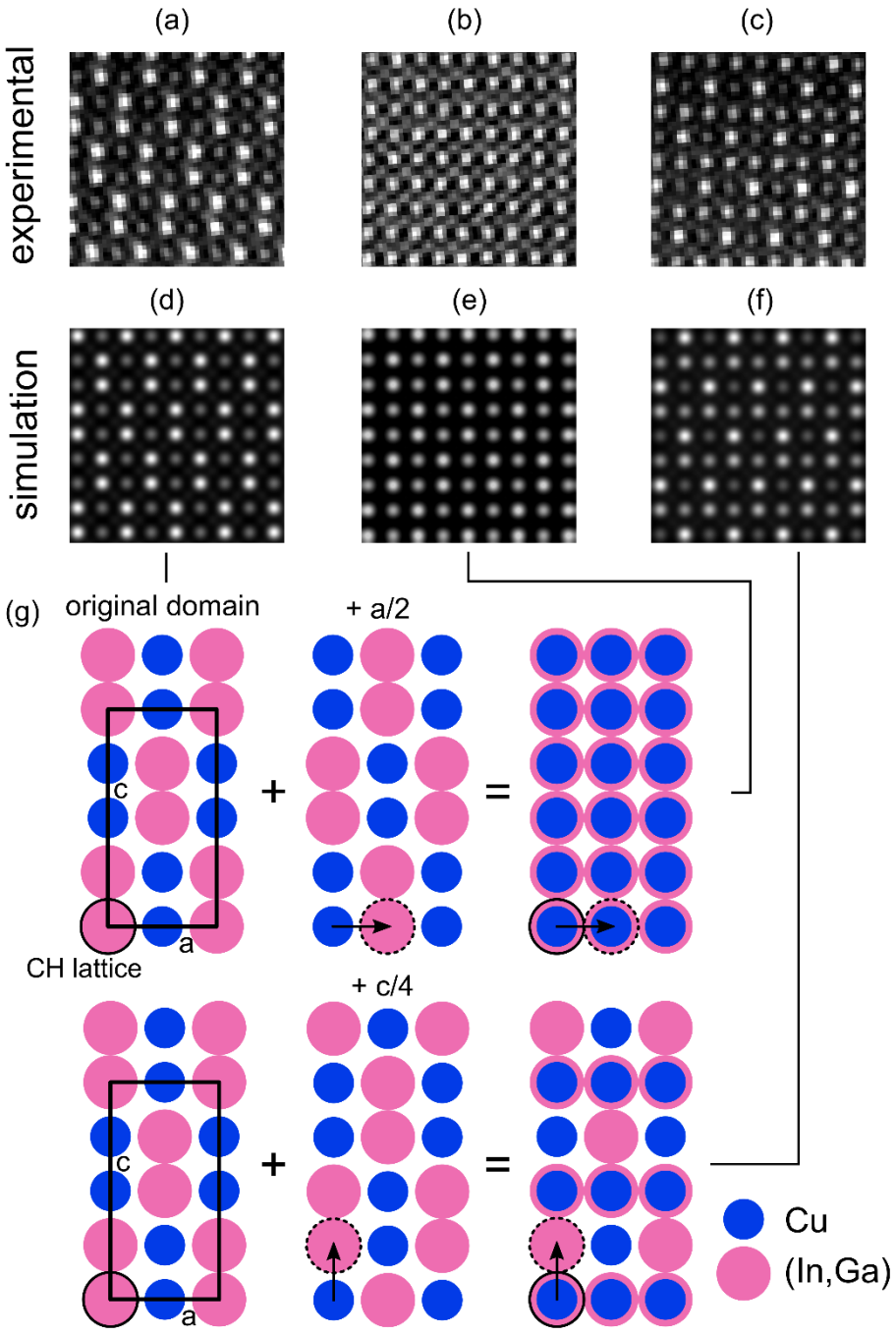

Figure 3: (a)(b)(c) experimental and (e)(f)(g) and simulated (Dr. Probe [21]) HR-STEM images of (a)(d) a defect-free CH lattice, (b)(e) of the superposition of two CH cation sublattice translated by a vector a/2 along [100], and (c)(f) of the superposition of two CH lattice translated by a vector c/4 along [001]. (g) Schematic of possible superposition of translated cation sublattice.

If the base domain and a “a/2-translated” domain are both present in the depth of the TEM lamella, all columns contain both Cu and III atoms, and thus appear in an intermediate shade of gray. Based on simulations, this should yield an HR image presented in Figure 3(e). This description precisely corresponds to an atomic ordering visible in the center of Figure 2(e),

and in Figure 3(b). Note that two “c/4 translation” would yield the same projected atomic ordering as one “a/2-translation”. We conclude from the considerations above that, in the Cu-poor sample, CH domains retaining cation coherence are small (<10nm), even compared to the TEM lamella thickness.

Interestingly, such cation-sublattice antiphase disorder implies the existence of extended defects corresponding to the boundary between such domains, which we will call cationic antiphase boundaries (CAPBs). In the following, the CAPB leading to an apparent ordering corresponding to the superposition of two “+a/2” CH domains will be called a/2-CAPB. Similarly, the CAPB leading to an apparent ordering corresponding to the superposition of two “+c/4” CH domains will be called c/4-CAPB. Both run on planes approximately parallel to the (100) plane of the STEM image, which allows two cationic CH domains to coexist in the direction of the lamella, i.e., the zone-axis. We argue that any kind of non-CH apparent ordering can be generated based on any weighted combination of “+a/2” and “+c/4” translations, or by including more than two CH domains in the depth of the lamella.

We therefore demonstrate that certain kinds of CAPB can be detected in the Cu-poor based on their HR-STEM fingerprint, which is a non-CH apparent ordering of the cation sublattice. In the following, we shift our attention to the Cu-rich epi-CIGS, to find additional clues of CAPBs presence.

5.3.2 Cation antiphase disorder in Cu-rich epi-CIGS

In the Cu-rich epi-CIGS sample, a nearly horizontal defect is visible in the center of the image in Figure 2(b). Taking a closer look at this defect, we find that it corresponds to a deviation from the CH in the sequence of cations in the [001] direction. We display in Figure 4(a) an HAADF-STEM image of the Cu-rich sample. We recall that III atoms appear brighter than Cu atoms, which allows us to identify the atomic species. In Figure 4(a), we can see two types of defects corresponding to a deviation of the CH atomic ordering. In the ideal CH cationic sublattice, III atoms and Cu atoms organize themselves in the doublets. In the [001] direction, the ideal ordering sequence of the cationic planes is *AABBAA*. The first type of defect is the one seen in the upper part of Figure 4(a), where a sequence of three III atoms or three Cu atoms is found instead of two, following *AAB**B**BAA* sequence. The second type of defect can be seen in two copies, in the lower part of the Figure 4(a). It corresponds to the sequence *AAB_AA*, where _ represents the missing cationic plane. So far, we only considered the projected distance onto the plane of the image. In the following, we consider the full extent of the third dimension to better describe the 3-dimentional structure of the defects.

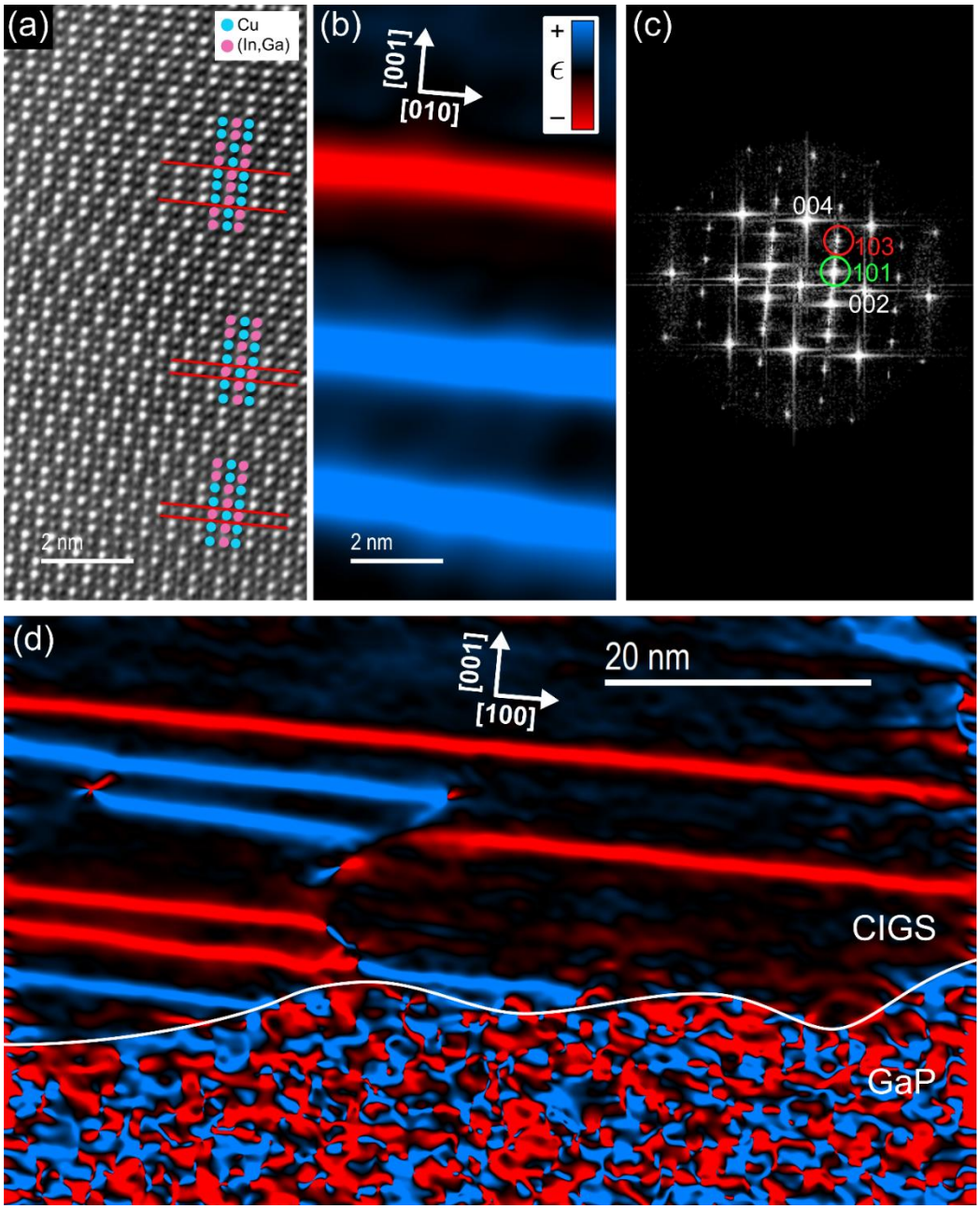

Figure 4: (a) HR-HAADF-STEM images and schematic of (100)-CAPB in the Cu-rich CIGS sample. (b) Corresponding GPA ε_{12} strain image when selecting (c) the CIGS(101) and CIGS(103) reflections exclusive to the CH phase on the Fast Fourier Transform. (d) Spatial distribution of (100)-CAPB defects in the Cu-rich CIGS layer at the CIGS/GaP interface as obtained by GPA.

Further analysis reveals that both defects of Figure 4(a) can be generated from a single symmetry operation. Let us consider a CH lattice and generate another CH lattice thanks to a rotation of 180° about the [100] zone-axis, with the two lattices being joined on the red (001) plane, as sketched in Figure 5(a-b), together with the corresponding HR simulation in Figure 5(c-d). This symmetry operation flips the direction of the [001] direction of the top lattice, relative to the bottom one. In the [010] zone-axis, Figure 5(d) precisely yields the *AAB_AA* defect observed experimentally in Figure 4(a). Similarly, in the [100] zone axis, Figure 5(d) generates the *AABBBAA* defect observed experimentally Figure 4(a). This demonstrates that both defects are indeed the same CAPB defect, seen through a different

zone axis. It can be conceptualized as a planar growth accident, from which a CH lattice starts to grow with its *c*-axis flipped, relative to the crystal underneath. In the following, we shall call such defects (001)-CAPBs, in reference to their strong tendency to run on (001) planes.

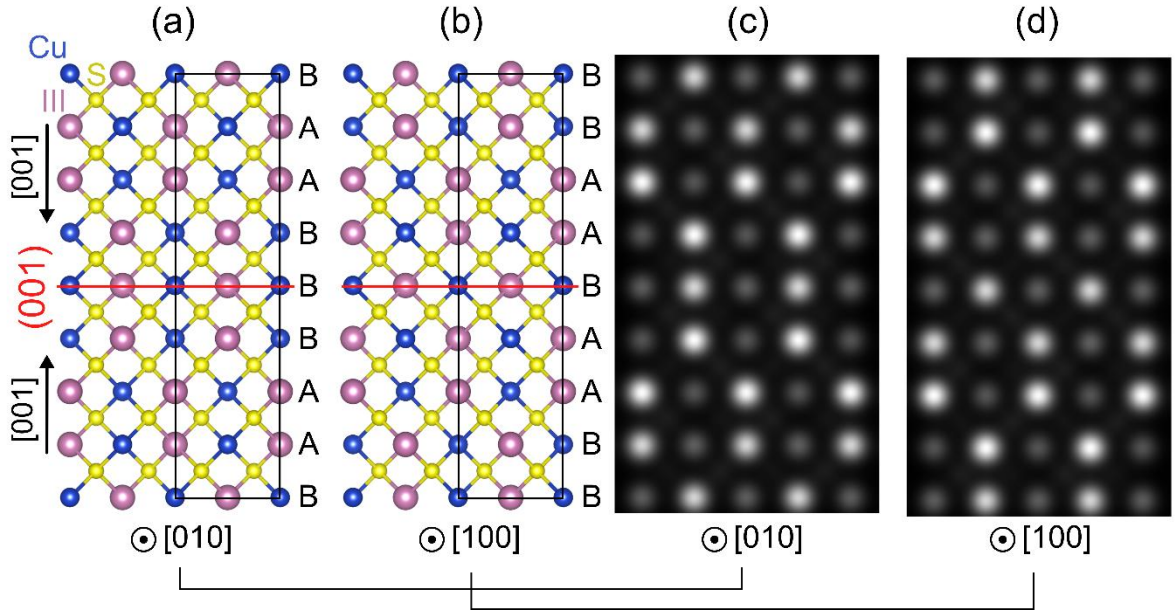

Figure 5: (a)(b) Vesta schematic and (c)(d) HAADF-STEM image simulation of two CH lattices sharing a symmetry corresponding to a rotation about [001], and joined along their (001) plane, as viewed in the (a)(c) [010] and (b)(d) [100] zone-axis

To highlight such CAPBs, we apply the geometric phase analysis (GPA). Here, we find that applying the GPA to (101) and (103) reflections is useful to highlight defects of the cation sublattice. Even if, in principle, GPA is used to map the strain in a crystalline sample, we underline that the GPA maps shown in this article cannot be interpreted as strain, for reasons developed in SI, Figure S4.

In the Cu-rich sample, the CH ordering is clearly visible, thanks to a better overall crystallinity. Therefore, we apply the method exposed in the previous paragraph to the Cu-rich sample. In Figure 4(f), we display a GPA map highlighting the position of the cationic *AAB**B**BAA* (in red) and *AAB_AA* (in blue). One can clearly see that the CAPBs are organized in the form of horizontal lines, following (001) planes. Therefore, near the CIGS/GaP interface, the CH domains sharing translational coherence are organized in layers of about 10nm in thickness. Since *AAB_AA* and *AAB**B**BAA* are, in fact, the same defect seen in a different zone-axis, they should be found in equal number if we assume an isotropic CIGS film, since [100] and [010] are equivalent. These defects seem to exist in large numbers in the vicinity of the CIGS/GaP interface. However, they are also visible in smaller numbers at the surface of the Cu-rich CIGS layer (see SI **Erreur ! Source du renvoi introuvable.**(a)(c)), which demonstrates that they are not confined to the CIGS/GaP interface exclusively.

In general terms, within the CH-CIGS layer, we observed CAPB defects corresponding to the boundary between CH domains sharing antiphase symmetry of the cation sublattice. These defects do not lead to a symmetry-breaking of the anion-to-cation ordering, unlike APD as

defined by the III-V/Si community. In the following section, we most specifically compare the Cu-poor and Cu-rich epi-CIGS samples, in regard to the CAPD.

5.3.3 Comparison of the cation antiphase disorder in the Cu-poor and Cu-rich epi-CIGS samples

In the Cu-poor sample, we do not clearly resolve the expected CH cation sublattice ordering over long distances. We detected apparent non-CH orderings, which were interpreted as a/2- and c/4-CAPBs running on planes approximately normal to the <100> zone-axis. In the Cu-rich sample, we do not find any evidence of a/2-CAPBs and c/4-CAPBs, as we do not detect any apparent non-CH orderings. This strongly suggests that a/2- and c/4-CAPB defects are only present in the Cu-poor epi-CIGS.

In the Cu-rich sample, we detected abrupt (001)-CAPB defects running on (001) planes. Even though these defects are easily spotted in the Cu-rich sample, most likely because of the absence of a/2-CAPB and c/4-CAPB defects, they can also be seen in the Cu-poor sample, in the inset of image Figure 2(d). This demonstrates that (001)-CAPB defects are present in the Cu-poor and in the Cu-rich epi-CIGS samples.

Table 1: Summary table of cation antiphase disorder in Cu-poor and Cu-rich epi-CIGS

Defect	(001)-CAPB	a/2-CAPB	c/4-CAPB
HR-STEM fingerprint	AAB_AA, AAB**B**BAA	"ZB-type" ordering	"Hex-type" ordering
Cu-rich	Present	Absent	Absent
Cu-poor	Present	Present	Present
Octet rule*	Respected	Violated	Violated

*Assuming an abrupt CAPB

When comparing the Cu-poor and Cu-rich CH crystals of Figure 2(e) and (b), the Cu-rich sample's CH seems to have longer-range cationic coherence. For the Cu-rich epi-CIGS samples, in the vicinity of the CIGS/GaP interface, the CH domains size in the [001] direction is limited by the presence of (001)-CAPBs to about 5 – 10nm (see Figure 4). Along <010>, i.e., along the plane of the STEM image, the CH domains may extend over larger distances of up to 100nm. Additionally, coherent CH domains are found to be larger (> 50 nm) in regions away from the interface like the surface, as shown in SI, Figure S4(a). On the other hand, the Cu-poor samples exhibits very small coherent CH domains of about 5 – 10nm in all directions, because of a higher density of CAPBs of the three kinds. In other words, the coherent CH crystal coherent cationic domains are larger in the Cu-rich sample than in the Cu-poor sample. This is in perfect agreement with Ref. [9] where diffraction peaks were much sharper in the Cu-rich sample. Table 1 summarizes the main conclusions of the comparison between the two samples.

These observations raise questions about recurrence of CAPB defects. A general comment arises from the comparison of the ionic radii of In^{3+} (0.62Å) and Cu^{1+} (0.6Å) cations in tetragonal coordination [32]. The similarity in ionic radii comforts the fact that Cu/In substitutions are possible. More importantly, it also supports the observation of CAPD in CIGS, as a higher cationic substitution probability may increase the likelihood of CAPD.

Furthermore, relatively low cation antiphase boundary energy of 0.26 J/m^2 for Se-based CH-$CuInSe_2$ have been found, which hints to a high likelihood of CAPB formation. In comparison, significantly higher antiphase boundary energies of 1.0 J/m^2 and 0.7 J/m^2 were observed in NiAl and FeAl, respectively [19]. Given that S-based CIGS also adopts the CH structure, one can similarly expect a low cation antiphase boundary energy.

5.4 Cation antiphase disorder and octet rule

Until now, we had projected distances onto (100) planes, and only considered the cation sublattice. In the following, we construct 3D crystal models to better visualize the chemical bonds at such CAPBs, assuming perfectly abrupt boundaries. For the (001)-CAPB defect of Figure 5, easily spotted in the Cu-rich sample, the corresponding model was already constructed. Regarding the CAPD within the depth of the lamella and across the image, which characterizes the Cu-poor sample, i.e., a/2-CAPBs and c/4-CAPBs, we have not yet created 3D crystal models. As displayed in Figure 6, c/4-CAPB defects can be obtained by taking the two rotated lattices of Figure 5(a-b) and joining them along (100) in the depth of the lamella. The result of this process in presented in Figure 6(b)(c). It yields an apparent ordering corresponding to the simulation in Figure 6(a) in the [001]-zone axis. As displayed in Figure 6(e)(f), another symmetry operation, consisting in substituting Cu with III atoms and vice versa, and placing the two CH lattices side by side along (100), allows us to generate the a/2-CAPB defects which yields an apparent ordering of Figure 6(d). In this model, a/2- and c/4-CAPBs are defects running abruptly on (100)/(010) type planes.

Such defects can be analyzed within the framework of the octet rule, which states that each S^{2-} anions must be bonded to two Cu^{+} cations and two III^{3+} cations to reach a s^2p^6 electron configuration. Deviation from the octet rule typically causes a large energy increase in the system [27]. In the following, we stress that we study perfectly abrupt boundaries, which is reasonable for (001)-CAPBs but may not account for the geometry of a/2-CAPBs and c/4-CAPBs. Indeed, the two latter may not form abrupt interfaces between CH domains.

In the first "+c/4" case, sketched in Figure 6(b-c), we find that S atoms placed at the defect boundary are either bonded to three III atoms and one Cu atom, or three Cu atoms and one III atom. In the second “+a/2” case, sketched in Figure 6(e-f), we find that S atoms placed at the defect boundary are either exclusively bonded to III atoms or to Cu atoms. In both former cases, the octet rule is locally violated, as marked in Table 1. This would suggest that such abrupt defects are energetically unfavorable. Indeed, since the violation of octet rule is energetically costly, single or complex 1D defects, like $2V_{Cu} + In_{Cu}$ [33], are expected to be generated. The violation of the octet rule would presumably be accommodated by the formation of defects and bonds distortions over several lattices, which would probably prevent such defects to form abrupt boundaries.

We observed that these energetically costly defects mostly appear in the Cu-poor sample. This suggests that they are metastable, and that elemental mobility in Cu-poor CIGS prevents these defects from being annihilated. Indeed, if an "a/2-translation" boundary meets another "a/2-translation" boundary, then the total translation corresponds to an entire cation sublattice parameter a, which restores the long-range symmetry of the crystal,

effectively annihilating the two defects. Another explanation would consist of postulating that 1D defects stable in Cu-poor CIGS may populate and stabilize such defects by solving the charge imbalances and locally supporting the octet rule. Thus, we argue that the presence of a/2- and c/4-CAPBs is associated with the existence of point defects and bond distortions, which may be harmful to the material's electronic properties.

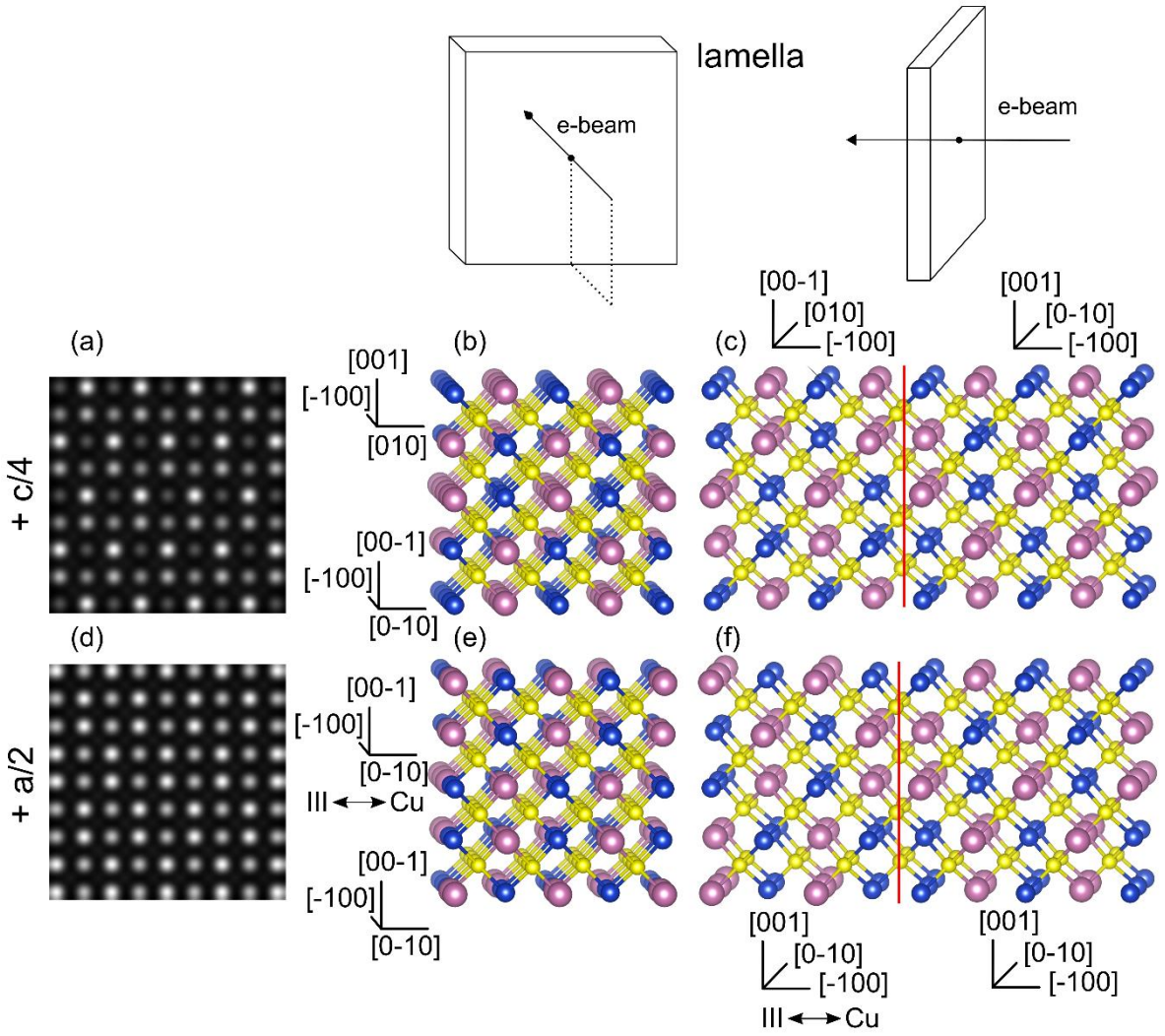

Figure 6: (a)(d) HR-STEM Dr. probe simulation in the [100] zone-axis of a crystal corresponding to (b)(c)(e) the superposition within the depth of the lamella of two CH domains. (b)(c) 3D atoms ordering seen in the (b) [100] and (c) [010] zone-axis, of a boundary between two lattices rotated about [100] by 180° (i.e., with opposite directions of the [001]). This generates a boundary corresponding to the "+c/4" ordering. (e)(f) 3D atoms ordering seen in the (e) [100] and (f) [010] zone-axis, of a boundary between two CH lattices. In the leftmost lattice the III and Cu atoms are swapped relative to the rightmost lattice. This generates a boundary corresponding to the "+a/2" ordering.

Despite the higher crystallinity of the Cu-rich sample [9], as compared to the Cu-poor sample, we detected a large number of specific (001)-CAPBs, stacked in the [001] direction (Figure 4). This suggests that such defects do not largely destabilize the CH structure. At the (001)-CAPB boundary defect in Figure 5(a-b), we do not detect any deviation from the octet

rule. This suggests that the generation of such defects does not come with a large energy cost, explaining their large density and their abrupt geometries.

6 Conclusion

In this article, we conducted a comparative analysis of two epi-CIGS samples grown on GaP/Si(001) under Cu-rich and Cu-poor conditions. Our investigations, utilizing electron diffraction and atomically resolved imaging, revealed that the CIGS crystal exhibits epitaxial growth for both growth conditions. In the Cu-poor sample exclusively, we found that the TS-$CuIn_5S_8$ secondary phase crystallizes at the CH-CIGS/GaP interface and shares an epitaxial relationship with the neighboring crystals. A close inspection of the differences in the HR-STEM image for the CH crystal of the Cu-poor and Cu-rich epi-CIGS samples allowed us to identify at least three kinds of CAPB defects in the cation sublattice. CAPB defects running along (100)/(010) planes were found to be exclusive to the Cu-poor epi-CIGS sample. We show that these abrupt CAPB defects in the cation sublattice lead to the violation of the octet rule. This most likely comes with a large energy cost, which may correlate with the formation of point defects to accommodate this apparent octet rule violation. This may mean that the latter boundaries are unstable or metastable, preventing them from adopting an abrupt geometry. On the other hand, CAPBs running along (001) planes are found for both compositions but are easily spotted in the Cu-rich sample due to better overall crystallinity. Such CAPBs, orthogonal to the [001] growth direction, do not violate the octet rule, which may not destabilize the system, explaining their abundance, even in the highly crystalline Cu-rich sample. Generally, we find that epi-CIGS is highly prone to the formation of CAPBs. We find that coherent CH domains size is below 5 nm in Cu-poor epi-CIGS. In the Cu-rich sample, we observe that the size of coherent CH domains in the <001> direction is between 5 nm to more than 100 nm, depending on the density of CAPBs running along (001) planes. Generally, we find that the growth of CIGS in Cu-rich conditions leads to a lower density of CAPBs, as compared to Cu-poor growth conditions.

7 Acknowledgements

This work is supported by the French National Research Agency project EPCIS (Grant no. ANR-20-CE05-0038). The authors are grateful to O. Hernandez for the fruitful discussions.

8 References

[1] M. Bär, W. Bohne, J. Röhrich, E. Strub, S. Lindner, M.C. Lux-Steiner, C.-H. Fischer, T.P. Niesen, F. Karg, Determination of the band gap depth profile of the penternary Cu(In(1−X)GaX)(SYSe(1−Y))2 chalcopyrite from its composition gradient, Journal of Applied Physics. 96 (2004) 3857–3860. https://doi.org/10.1063/1.1786340.

[2] F. Martinho, Challenges for the future of tandem photovoltaics on the path to terawatt levels: A technology review, (2021).

[3] T.P. White, N.N. Lal, K.R. Catchpole, Tandem Solar Cells Based on High-Efficiency c-Si Bottom Cells: Top Cell Requirements for >30% Efficiency, IEEE Journal of Photovoltaics. 4 (2014) 208–214. https://doi.org/10.1109/JPHOTOV.2013.2283342.

[4] O. Durand, A. Létoublon, C. Cornet, A. Rolland, A. Zhou, S. Boyer-Richard, F. Fan, N. Barreau, E. Gautron, M. Balestrieri, D. Coutancier, D. Lincot, CIGS growth on a

GaP/Si(001) platform : towards CIGS/Si tandem solar cells, 2021. https://hal.archives-ouvertes.fr/hal-03032879 (accessed February 9, 2021).
[5] N. Barreau, E. Bertin, A. Crossay, O. Durand, L. Arzel, S. Harel, T. Lepetit, L. Assmann, E. Gautron, D. Lincot, Investigation of co-evaporated polycrystalline Cu(In,Ga)S2 thin film yielding 16.0 % efficiency solar cell, EPJ Photovolt. 13 (2022) 17. https://doi.org/10.1051/epjpv/2022014.
[6] S. Shukla, M. Sood, D. Adeleye, S. Peedle, G. Kusch, D. Dahliah, M. Melchiorre, G.-M. Rignanese, G. Hautier, R. Oliver, S. Siebentritt, Over 15% efficient wide-band-gap Cu(In,Ga)S2 solar cell: Suppressing bulk and interface recombination through composition engineering, Joule. 5 (2021) 1816–1831. https://doi.org/10.1016/j.joule.2021.05.004.
[7] S. Knack, Copper-related defects in silicon, Materials Science in Semiconductor Processing. 7 (2004) 125–141. https://doi.org/10.1016/j.mssp.2004.06.002.
[8] A.R. Jeong, S.B. Choi, W.M. Kim, J.-K. Park, J. Choi, I. Kim, J. Jeong, Electrical analysis of c-Si/CGSe monolithic tandem solar cells by using a cell-selective light absorption scheme, Scientific Reports. 7 (2017) 15723. https://doi.org/10.1038/s41598-017-15998-y.
[9] E. Bertin, O. Durand, A. Létoublon, C. Cornet, L. Arzel, L. Choubrac, R. Bernard, É. Gautron, S. Harel, M. Jullien, T. Rohel, L. Assmann, N. Barreau, Unveiling the role of copper content in the crystal structure and phase stability of epitaxial Cu(In,Ga)S2 films on GaP/Si(001), Materials Science in Semiconductor Processing. 166 (2023) 107685. https://doi.org/10.1016/j.mssp.2023.107685.
[10] N. Barreau, O. Durand, E. Bertin, A. Létoublon, C. Cornet, P. Tsoulka, E. Gautron, D. Lincot, Epitaxial growth of CIGSe layers on GaP/Si(001) pseudo-substrate for tandem CIGSe/Si solar cells, Solar Energy Materials and Solar Cells. 233 (2021) 111385. https://doi.org/10.1016/j.solmat.2021.111385.
[11] Y. Takagi, Y. Furukawa, A. Wakahara, H. Kan, Lattice relaxation process and crystallographic tilt in GaP layers grown on misoriented Si(001) substrates by metalorganic vapor phase epitaxy, Journal of Applied Physics. 107 (2010) 063506. https://doi.org/10.1063/1.3310479.
[12] H. Emmer, C.T. Chen, R. Saive, D. Friedrich, Y. Horie, A. Arbabi, A. Faraon, H.A. Atwater, Fabrication of Single Crystal Gallium Phosphide Thin Films on Glass, Sci Rep. 7 (2017) 4643. https://doi.org/10.1038/s41598-017-05012-w.
[13] Ioffe Institute, New Semiconductor Materials. Characteristics and Properties, (n.d.). http://www.ioffe.ru/SVA/ (accessed December 12, 2022).
[14] Ioffe Institute, Basic Parameters of Gallium Phosphide (GaP), (n.d.). https://www.ioffe.ru/SVA/NSM/Semicond/GaP/basic.html (accessed September 22, 2022).
[15] R. Hunger, C. Pettenkofer, R. Scheer, Surface properties of (111), (001), and (110)-oriented epitaxial CuInS2/Si films, Surface Science. 477 (2001) 76–93. https://doi.org/10.1016/S0039-6028(01)00707-5.
[16] M. Turcu, I.M. Kötschau, U. Rau, Composition dependence of defect energies and band alignments in the Cu(In1−xGax)(Se1−ySy)2 alloy system, Journal of Applied Physics. 91 (2002) 1391–1399. https://doi.org/10.1063/1.1432126.
[17] B. Tseng, S. Lin, G. Gu, W. Chen, Elimination of orientation domains and antiphase domains in the epitaxial films with chalcopyrite structure, Journal of Applied Physics. 79 (1996) 1391–1396. https://doi.org/10.1063/1.361038.

[18] D. Abou-Ras, A. Nikolaeva, M. Krause, L. Korte, H. Stange, R. Mainz, E. Simsek Sanli, P.A. van Aken, T. Sugaya, J. Nishinaga, Optoelectronic Inactivity of Dislocations in Cu(In,Ga)Se2 Thin Films, Physica Status Solidi (RRL) – Rapid Research Letters. 15 (2021) 2100042. https://doi.org/10.1002/pssr.202100042.

[19] N.I. Medvedeva, E.V. Shalaeva, M.V. Kuznetsov, M.V. Yakushev, First-principles study of deformation behavior and structural defects in $\mathrm{Cu}\mathrm{In}{\mathrm{Se}}_{2}$ and $\mathrm{Cu}(\mathrm{In},\mathrm{Ga}){\mathrm{Se}}_{2}$, Phys. Rev. B. 73 (2006) 035207. https://doi.org/10.1103/PhysRevB.73.035207.

[20] T. Quinci, J. Kuyyalil, T.N. Thanh, Y.P. Wang, S. Almosni, A. Létoublon, T. Rohel, K. Tavernier, N. Chevalier, O. Dehaese, N. Boudet, J.F. Bérar, S. Loualiche, J. Even, N. Bertru, A.L. Corre, O. Durand, C. Cornet, Defects limitation in epitaxial GaP on bistepped Si surface using UHVCVD–MBE growth cluster, Journal of Crystal Growth. 380 (2013) 157–162. https://doi.org/10.1016/j.jcrysgro.2013.05.022.

[21] J. Barthel, Dr. Probe: A software for high-resolution STEM image simulation, Ultramicroscopy. 193 (2018) 1–11. https://doi.org/10.1016/j.ultramic.2018.06.003.

[22] E. Rauch, K. Barmak, J. Ganesh, P. Ferreira, A. Darbal, D. Choi, T. Sun, B. Yao, K. Coffey, S. Nicolopoulos, Automated Crystal Orientation and Phase Mapping for Thin Film Applications by Transmission Electron Microscopy, Microsc Microanal. 17 (2011) 1086–1087. https://doi.org/10.1017/S1431927611006301.

[23] H. Du, GPA: Geometric Phase Analysis software, 2018. https://doi.org/10.13140/RG.2.2.26792.67845.

[24] Peter Schlossmacher, Dmitri O. Klenov, Bert Freitag, Sebastian von Harrach and Andy Steinbach, Nanoscale Chemical Compositional Analysis with an Innovative S/TEM-EDX System, Wiley Analytical Science. (n.d.). https://analyticalscience.wiley.com/do/10.1002/micro.504 (accessed May 9, 2023).

[25] X. Gu, T. Furuhara, W. Zhang, PTCLab: Free and open-source software for calculating phase transformation crystallography, Journal of Applied Crystallography. 49 (2016). https://doi.org/10.1107/S1600576716006075.

[26] O.L. Krivanek, M.F. Chisholm, V. Nicolosi, T.J. Pennycook, G.J. Corbin, N. Dellby, M.F. Murfitt, C.S. Own, Z.S. Szilagyi, M.P. Oxley, S.T. Pantelides, S.J. Pennycook, Atom-by-atom structural and chemical analysis by annular dark-field electron microscopy, Nature. 464 (2010) 571–574. https://doi.org/10.1038/nature08879.

[27] J.K. Larsen, K.V. Sopiha, C. Persson, C. Platzer-Björkman, M. Edoff, Experimental and Theoretical Study of Stable and Metastable Phases in Sputtered CuInS2, Advanced Science. 9 (2022) 2200848. https://doi.org/10.1002/advs.202200848.

[28] C. Cornet, S. Charbonnier, I. Lucci, L. Chen, A. Létoublon, A. Alvarez, K. Tavernier, T. Rohel, R. Bernard, J.-B. Rodriguez, L. Cerutti, E. Tournié, Y. Léger, M. Bahri, G. Patriarche, L. Largeau, A. Ponchet, P. Turban, N. Bertru, Zinc-blende group III-V/group IV epitaxy: Importance of the miscut, Phys. Rev. Materials. 4 (2020) 053401. https://doi.org/10.1103/PhysRevMaterials.4.053401.

[29] Y. Ping Wang, A. Letoublon, T. Nguyen Thanh, M. Bahri, L. Largeau, G. Patriarche, C. Cornet, N. Bertru, A. Le Corre, O. Durand, Quantitative evaluation of microtwins and antiphase defects in GaP/Si nanolayers for a III–V photonics platform on silicon using a laboratory X-ray diffraction setup, J Appl Cryst. 48 (2015) 702–710. https://doi.org/10.1107/S1600576715009954.

[30] S. Senz, A. Graff, C. Teichert, M. Zimnol, H. Sieber, S.K. De, H.P. Oepen, D. Hesse, J. Kirschner, U.M. Gösele, Reactive Growth and Properties of Epitaxial Fe-Mg-O Spinel Films on (100) MgO, MRS Online Proceedings Library. 474 (1997) 277–282. https://doi.org/10.1557/PROC-474-277.

[31] H. Tabata, E. Ishii, H. Okuda, Cation antiphase boundaries in ionic crystals based on anion close packing, Journal of Crystal Growth. 52 (1981) 956–962. https://doi.org/10.1016/0022-0248(81)90405-X.

[32] R.D. Shannon, Revised effective ionic radii and systematic studies of interatomic distances in halides and chalcogenides, Acta Cryst A. 32 (1976) 751–767. https://doi.org/10.1107/S0567739476001551.

[33] P. Yang, L.-J. Shi, J.-M. Zhang, G.-B. Liu, S.A. Yang, W. Guo, Y. Yao, Tuning to the band gap by complex defects engineering: insights from hybrid functional calculations in CuInS2, J. Phys. D: Appl. Phys. 51 (2017) 025105. https://doi.org/10.1088/1361-6463/aa9c17.

[34] A. Thomere, C. Guillot-Deudon, M. Caldes, R. Bodeux, N. Barreau, S. Jobic, A. Lafond, Chemical crystallographic investigation on Cu2S-In2S3-Ga2S3 ternary system, Thin Solid Films. 665 (2018) 46–50. https://doi.org/10.1016/j.tsf.2018.09.003.

[35] M.J. Hÿtch, E. Snoeck, R. Kilaas, Quantitative measurement of displacement and strain fields from HREM micrographs, Ultramicroscopy. 74 (1998) 131–146. https://doi.org/10.1016/S0304-3991(98)00035-7.

[36] J.J.P. Peters, R. Beanland, M. Alexe, J.W. Cockburn, D.G. Revin, S.Y. Zhang, A.M. Sanchez, Artefacts in geometric phase analysis of compound materials, Ultramicroscopy. 157 (2015) 91–97. https://doi.org/10.1016/j.ultramic.2015.05.020.